Structural control on the 2018 and 2019 Hualien earthquakes in Taiwan

Genti Toyokuni [a,*], Dapeng Zhao [a], Kate Huihsuan Chen [b]

[a] Department of Geophysics, Graduate School of Science, Tohoku University, Sendai 980-8578, Japan
[b] Department of Earth Sciences, National Taiwan Normal University, Taipei 11677, Taiwan

ARTICLE INFO

ABSTRACT

The 2018 Mw 6.4 Hualien earthquake and the 2019 Mw 6.1 Hualien earthquake occurred beneath the eastern coast of Taiwan, at depths of $<\sim20$ km. The two earthquakes caused a total of 18 fatalities and widespread damage to infrastructures, especially in the Hualien City. To better understand the generating mechanism of the damaging earthquakes, we conducted seismic tomography to determine high-resolution 3-D models of P and S wave velocity (V_P, V_S) and Poisson's ratio (σ) in the source zone. We used 334,645 P- and 238,581 S-wave arrival times of 20,825 local earthquakes ($1.5 \leq M_L \leq 6.9$) recorded at 47 seismic stations in Taiwan. Our results show that the hypocenters of the two Hualien mainshocks are located at a sharp vertical boundary where seismic velocity and Poisson's ratio change drastically in the horizontal direction, which corresponds to the location of the Longitudinal Valley Fault and its branches. Furthermore, the hypocenters are located right above a high-σ anomaly that is connected to the estimated upper boundary of the subducting Philippine Sea slab, which may reflect ascending fluids dehydrated from the slab. These results suggest that the 2018 and 2019 Hualien earthquakes were triggered by ascending fluids from the slab dehydration, invading into active faults that may be the northern extension of the Longitudinal Valley Fault.

1. Introduction

At 23:50 local time on 6 February 2018, the 2018 Hualien earthquake (Mw 6.4) occurred at 18 km NE of Hualien city, eastern Taiwan (Fig. 1). According to the Taiwan Central Weather Bureau (CWB), its hypocenter is located at 24.10°N and 121.73°E with a focal depth of 6.3 km (https://scweb.cwb.gov.tw/zh-tw/earthquake/details/2018020623 504162022). The peak ground acceleration was observed to be 484 gal in Taroko near Hualien, causing 17 fatalities and 285 injuries. One year later, at 13:01 local time on 18 April 2019, the 2019 Hualien earthquake (Mw 6.1) occurred at 24.05°N and 121.56°E with a focal depth of 20.3 km (https://scweb.cwb.gov.tw/zh-tw/earthquake/details/2019041813 010763031), which caused one fatality and 16 injuries.

Taiwan has very complex geological and tectonic features, due to strong interactions between the Philippine Sea (PHS) plate and the Eurasian plate (Fig. 1a). The PHS plate is subducting beneath the Eurasian plate in northeast Taiwan towards NNW from the Ryukyu Trench, with a convergence rate of ~80 mm/year (Seno et al., 1993; Yu et al., 1997), forming the Ryukyu Arc. On the other hand, the Eurasian plate is subducting beneath the PHS plate in South Taiwan towards the east from the Manila Trench, forming the Luzon Arc (Chai, 1972). The

ongoing complex plate convergence has caused a young orogeny on inland Taiwan since 6.5–5.0 Ma (Teng, 1990; Lin and Watts, 2002), generating geological structures with a dominant strike direction in NNE-SSW. The Taiwan orogenic belt is composed of four major geological provinces, *i.e.*, the Coastal Plain, the Western Foothills, the Central Range, and the Coastal Range, which are well bordered by surface active faults (Ho, 1988). The Coastal Plain (I in Fig. 1a) consists of the Quaternary sedimentary deposits that form a part of the current foreland basin. The Western Foothills (II in Fig. 1a) contain the Oligocene to the Pleistocene clastic sediments stacked by a NW-trending fold-and-thrust belt. The Central Range (III in Fig. 1a) is an active mountain belt containing the Tertiary submetamorphic rocks and the pre-Tertiary metamorphic complex. The Coastal Range (IV in Fig. 1a) is considered as the colliding Luzon volcanic arc composed of the Miocene to the Pliocene andesitic arc rocks overlain by imbricated thrust sheets.

Because the major surface rupture occurred along the Milun fault (Huang et al., 2019; Lin et al., 2019; Wu et al., 2019; Yamada et al., 2020), the 2018 Hualien event is believed to take place at the northern extension of the Longitudinal Valley Fault (LVF) that borders the Central Range and the Coastal Range. According to the Harvard CMT solutions (https://www.globalcmt.org/), its focal mechanism (Fig. 1b) has two
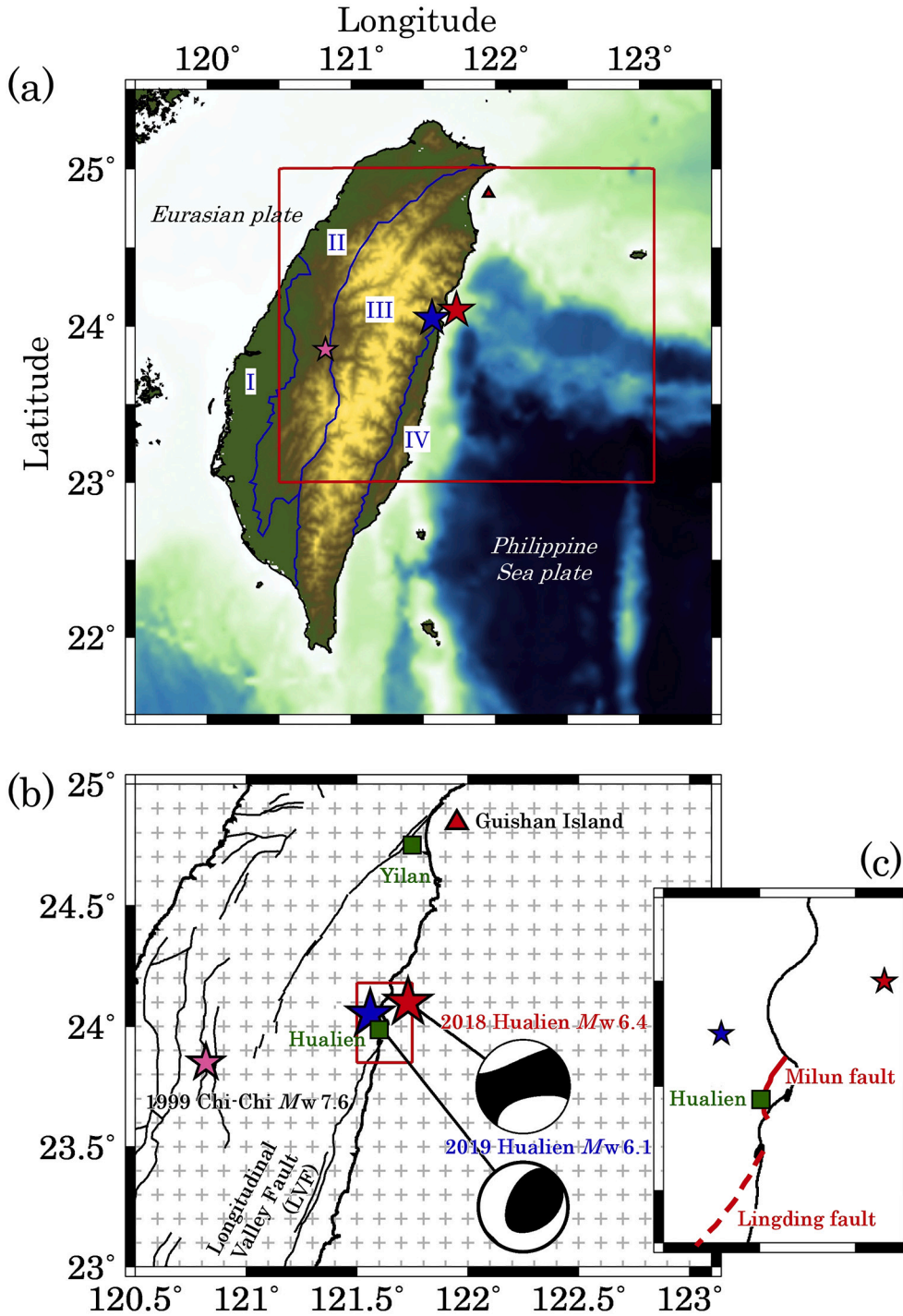

Fig. 1. (a) The surface topography and tectonic setting in and around Taiwan. The red box shows our study region that is enlarged in (b). The red star represents the 2018 Hualien earthquake (*M*w 6.4) that occurred on 6 February 2018. The blue star represents the 2019 Hualien earthquake (*M*w 6.1) that occurred on 18 April 2019. I, II, III, and IV indicate the Coastal Plain, the Western Foothills, the Central Range, and the Coastal Range, respectively. (b) The present study region. The two Hualien earthquake epicenters are shown with the Harvard CMT focal-mechanism solutions. The pink star denotes the epicenter of the 1999 Chi-Chi earthquake (*M*w 7.6). The curved lines in the inland areas denote active faults. The gray crosses represent the grid nodes set up for tomographic inversions. The red triangle denotes the Guishan Island, the only active volcano in Taiwan. The green squares show Hualien and Yilan cities. The red box shows a region enlarged in (c). (c) A map showing the relationship between the two large events and the Milun and Lingding faults (Huang and Huang, 2018). (For interpretation of the references to colour in this figure legend, the reader is referred to the web version of this article.)
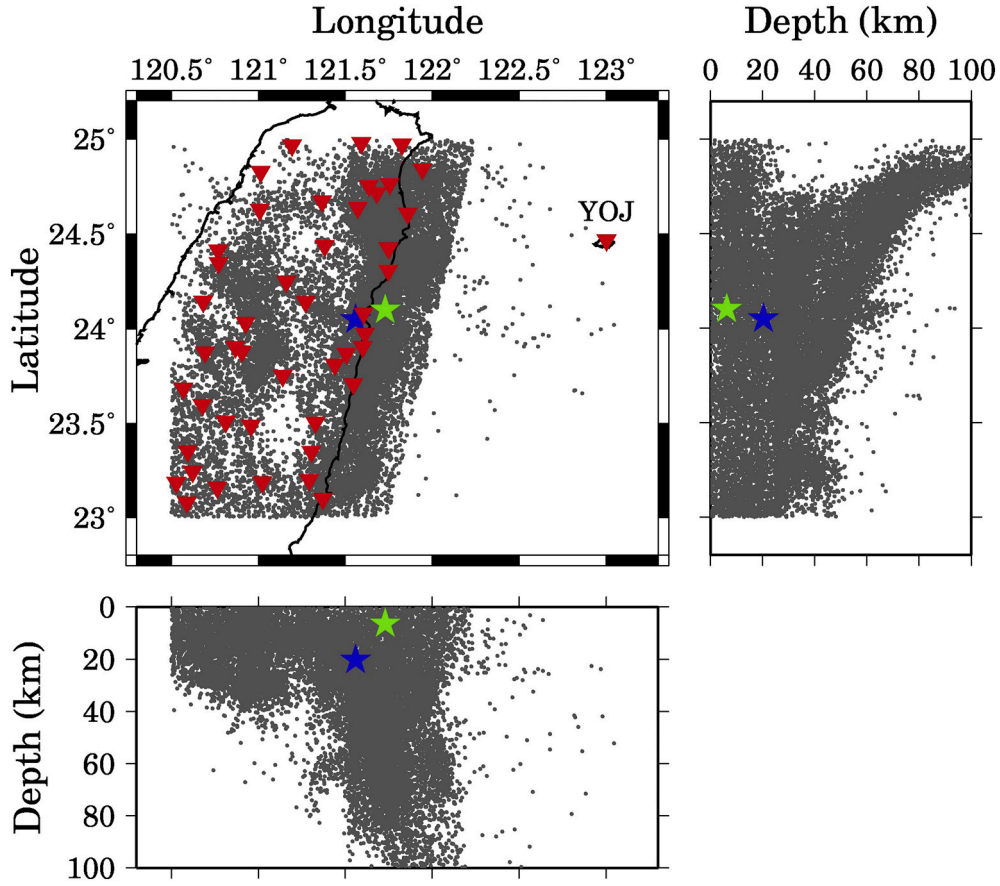
Fig. 2. Distribution of the 20,825 earthquakes (gray dots) and the 47 seismic stations (red inverse triangles) used in this study. The green and blue stars denote the 2018 and 2019 Hualien earthquakes, respectively. YOJ: station code for Yonagunijima Island, Japan. (For interpretation of the references to colour in this figure legend, the reader is referred to the web version of this article.)

nodal planes with (strike, dip, rake) = (212°, 54°, 28°) and (105°, 68°, 141°), characterized by a significant non-double-couple component (double-couple (DC): 86.1%; isotropic (ISO): 0.0%; compensated linear vector dipole (CLVD): 13.9%), indicating a complex rupture process. Recent studies of the rupture process of the 2018 event show that its rupture started on an unknown offshore fault on the northern side, propagated southward, and jumped to the Milun fault and the Lingding fault (Fig. 1c), causing strong ground motion and serious surface deformation (Huang and Huang, 2018; Lee et al., 2019; Lo et al., 2019; Tung et al., 2019). The Harvard CMT focal mechanism of the 2019 event (Fig. 1b) has two nodal planes with (strike, dip, rake) = (68°, 40°, 128°) and (202°, 60°, 63°), and also contains a significant non-double-couple component (DC: 73.8%; ISO: 0.1%; CLVD: 26.1%).

These results suggest the complex rupture processes and heterogeneous structures in the source zone of the two earthquakes. Near the source zone, the interaction between the PHS plate and the Eurasian plate changes from collision to subduction. Such transition leads to complex co-seismic slip on multiple faults during and after the mainshocks. To clarify the seismogenesis, a better understanding of the detailed 3-D structure of the crust and upper mantle in the source zone is needed.

Seismic tomography is a powerful tool for imaging structural heterogeneities in the crust and upper mantle, and many tomographic studies have been made for the Taiwan region (*e.g.*, Wang et al., 2006; Wu et al., 2009; Huang et al., 2014; Toyokuni et al., 2016; Wang and Kao, 2019; Fan and Zhao, 2021). In this study, we use a large number of high-quality arrival-time data to determine high-resolution tomography of the crust and upper mantle beneath the Hualien earthquake area, which sheds new light on the causal mechanism of these damaging earthquakes.

2. Data and method

The target region of this study is within the latitude range 23.0°–25.0°N and longitude range 120.5°–123.1°E (Fig. 1b). *P* and *S* wave arrival-time data from 20,825 local earthquakes are used for our tomographic inversion, which were recorded by a dense seismic network operated by the CWB (Fig. 2). These local events occurred within the target region during a period from January 2000 to December 2011. Although the original CWB data contains 181,738 local earthquakes, further event selection is conducted with a procedure similar to that by Toyokuni et al. (2016). This procedure is summarized as follows. (1) After relocating all the local events, we only selected those events recorded at five or more stations, with absolute travel-time residuals $|T_{obs} - T_{cal}| \leq 1.6$ s for *P*-wave data, and ≤ 2.0 s for *S*-wave data, where T_{obs} and T_{cal} are the observed and theoretical arrival times, respectively. After this processing, we got 164,182 events. (2) The events with $M_L \geq 1.5$ and uncertainties of the origin time ≤ 0.3 s, focal latitude $\leq 0.015°$, focal longitude $\leq 0.015°$, and focal depth ≤ 2.5 km are further selected (see Fig. S1). After this processing, we got 85,606 events. (3) The target region was divided into $0.05° \times 0.05° \times 2.5$ km cubic blocks at depths ≤ 25 km, and $0.01° \times 0.01° \times 1.0$ km cubic blocks at depths > 25 km, and only one event in each block with the maximum number of arrival-time data was selected. This process leads to a uniform distribution of hypocenters and good ray coverage in the study volume. After this processing, 24,029 events remain in the data set. (4) When the events are located offshore from a line passing through points (latitude, longitude) = (23.00°, 121.75°) and (25.00°, 122.25°), we only select those events
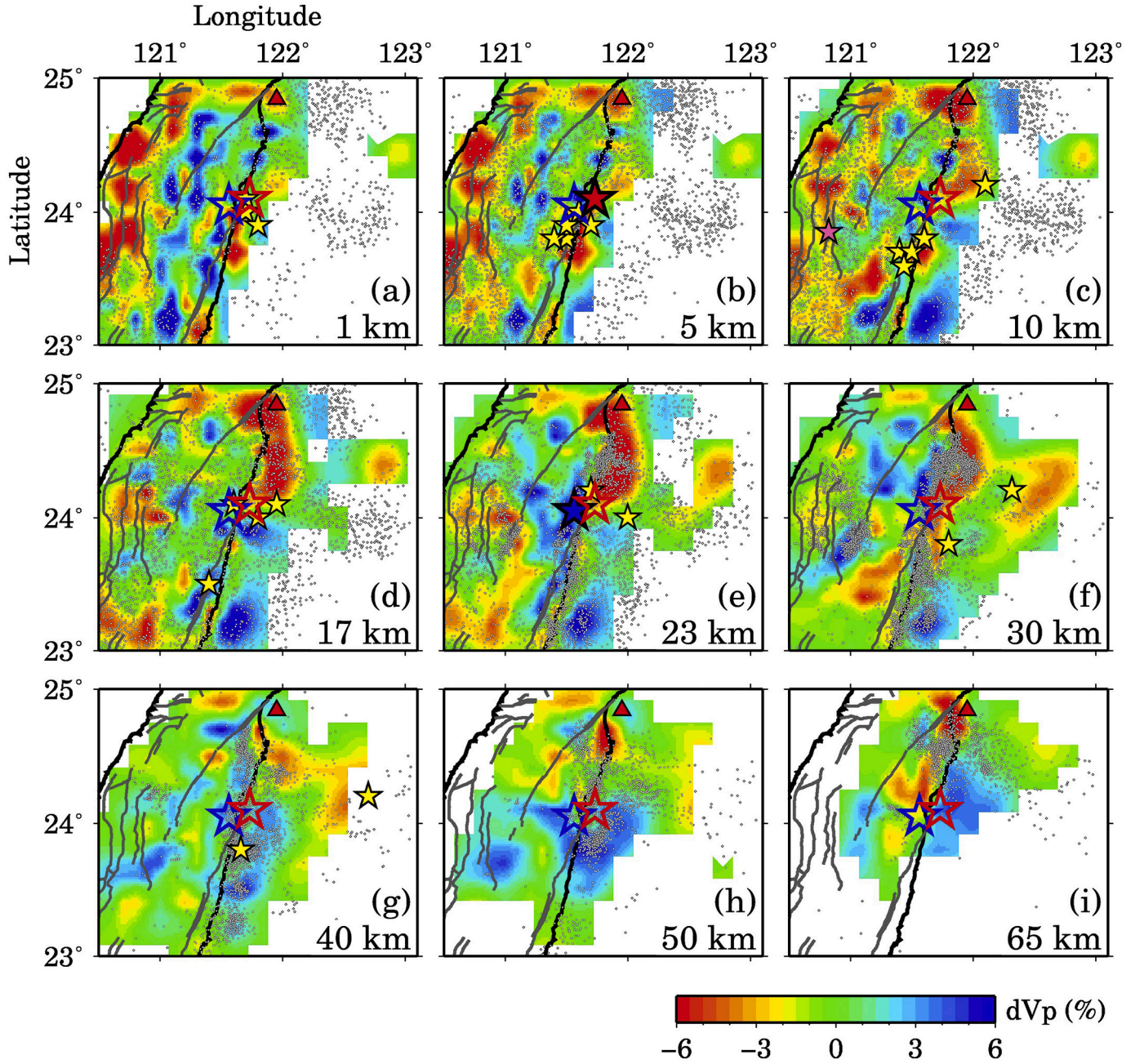
Fig. 3. Map views of *P*-wave velocity (V_P) tomography. The layer depth is shown at the lower-right corner of each map. The red and blue colours denote low and high V_P perturbations, respectively, whose scale is shown at the bottom. Areas with ray hit counts <50 are masked in white. The red and blue stars denote the epicenters of the 2018 and 2019 Hualien earthquakes, respectively. Solid stars are used on the closest layer to the focal depths; open stars are used on other layers. The pink star denotes the epicenter of the 1999 Chi-Chi earthquake. The yellow stars denote the epicenters of damaging earthquakes (*M* 5.7–8.3) that occurred in the Hualien area during 1908–2015 (Table S1). The gray dots denote local seismicity within a 10-km depth range of each layer. The curved gray lines denote active faults on the surface. The red triangle denotes the Guishan active volcano. (For interpretation of the references to colour in this figure legend, the reader is referred to the web version of this article.)

recorded at an offshore station YOJ (Fig. 2) to eliminate the poorly located offshore events. We finally extracted 20,825 events with $1.5 \leq M_L \leq 6.9$ and focal depths <100 km. These events generated 334,645 *P*-wave and 238,581 *S*-wave arrival times recorded at 47 seismic stations in North Taiwan (Fig. 2, see also Fig. S2).

We apply the seismic tomography method of Zhao et al. (1992) to determine 3-D *P*- and *S*-wave velocity (V_P, V_S) models of the target region. This method discretizes the structure using a 3-D grid arranged in the study volume. The grid interval is 0.1° in both the latitudinal and longitudinal directions (Fig. 1b). In the vertical direction, grid meshes are set at depths of 1, 5, 10, 17, 23, 30, 40, 50, 65, and 90 km beneath the

target region (see Fig. S3). Hypocentral parameters of the local events and velocity perturbations at the 3-D grid nodes from a 1-D starting model are taken as unknown parameters that are solved iteratively.

The starting 1-D velocity model (Fig. S4) for the tomographic inversion is similar to those of previous studies (*e.g.*, Zhao et al., 1992; Wang et al., 2006; Toyokuni et al., 2016). The geometry of the Moho discontinuity beneath Taiwan Island derived by Hsu et al. (2011) is taken into account (Fig. S5). The depth of the Conrad discontinuity is taken to be a half of the Moho depth. The subducting Eurasian and PHS slabs are not considered in the starting velocity model, because their geometries are not well known in the study region. Ustaszewski et al.
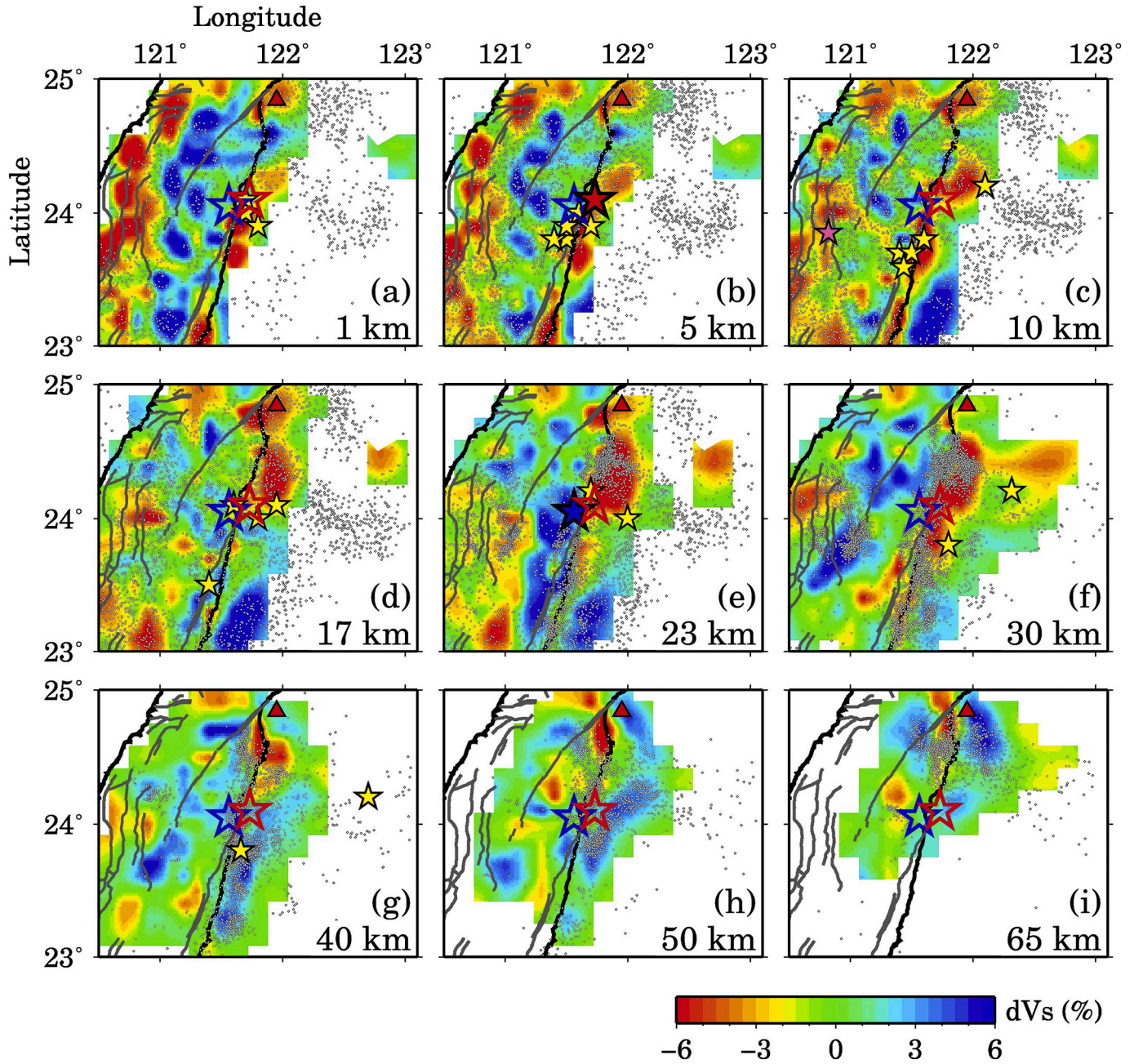
Fig. 4. The same as Fig. 3 but for *S*-wave velocity (V_S) tomography. (For interpretation of the references to colour in this figure legend, the reader is referred to the web version of this article.)

(2012) estimated general geometries of the upper boundaries of the subducting Eurasian and PHS slabs from seismicity and isovelocity surfaces of their tomography model, which are visible in a part of the study region. In this work we integrate the slab upper boundaries by interpolation (Fig. S6), which are only used as a rough reference to the slab locations and geometries when we show our tomographic images in vertical cross-sections.

The tomographic inversion is conducted using the LU (lower-upper) decomposition algorithm with damping and smoothing regularizations. The 3-D V_P and V_S models are determined simultaneously in the inversion. Using the resulting V_P and V_S models, we further determine the Poisson's ratio (σ) image using the relation $(V_P / V_S)^2 = 2(1-\sigma)/(1-2\sigma)$ (Zhao et al., 1996).

3. Results

Our tomographic images show significant lateral variations of up to 6% for V_P and V_S, and 10% for σ in the crust and uppermost mantle beneath the study region (Figs. 3–5). The seismic ray coverage and the ray hit count, *i.e.*, the number of rays sampling around a grid node, are shown in Figs. S7 – S9. Reliable results are expected in areas with a hit count ≥ 50, and the less reliable areas are masked in white when we show our tomographic images.

In the upper crust (depth ≤ 10 km), the most remarkable feature is low-V_P, low-V_S and high-σ anomalies in areas with known active faults and sedimentary layers in the northwestern and easternmost parts of Taiwan. In contrast, high-V_P, high-V_S and low-σ anomalies become wider in the lower crust and in the uppermost mantle. The source zone of the 2018 and 2019 Hualien earthquakes is located in a prominent area
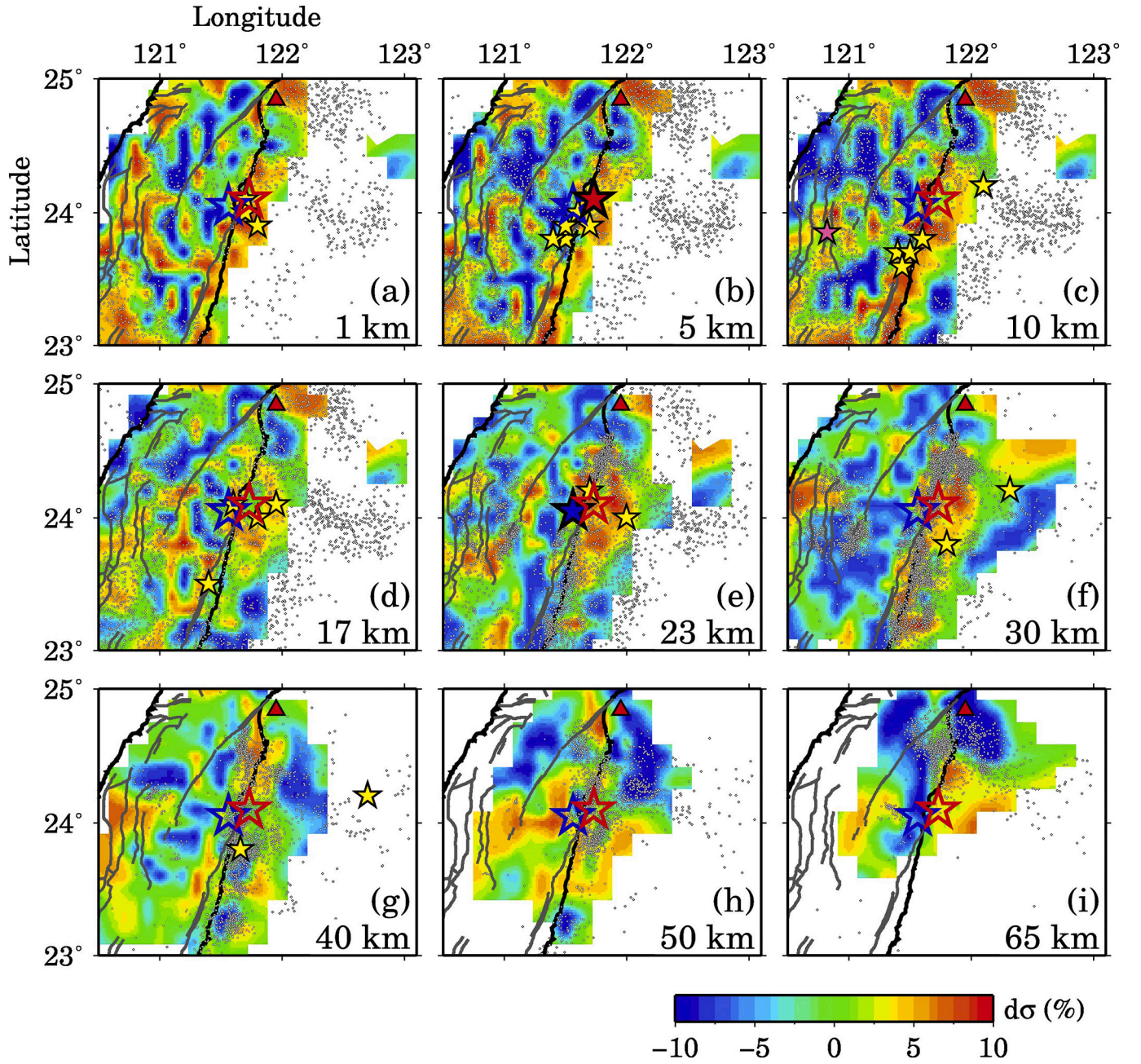
Fig. 5. The same as Fig. 3 but for the Poisson's ratio (σ) images. The red and blue colours denote high and low values of Poisson's ratio, respectively. (For interpretation of the references to colour in this figure legend, the reader is referred to the web version of this article.)

where seismic velocity and Poisson's ratio change drastically in the horizontal directions, reflecting distinct differences in the geological structure between the Central Range and the Coastal Range. In addition, low-V_P and low-V_S anomalies are also prominent beneath the Guishan Island where the only active volcano in Taiwan exists.

In vertical cross-sections (Figs. 6 and 7, see also Figs. S10 − S15), we can also clearly see the strong lateral and vertical structural heterogeneities beneath the study region. It is notable that the major active faults such as the LVF, Lishan Fault, and other faults separating geological blocks are well imaged as high-σ anomalies, which indicates accuracy and reliability of our results. These major faults are almost vertical or shaped like décollement, corresponding well to the known geological features (e.g., Chen et al., 2018, see Fig. 7). At the shallow depths (≤ 20 km), the Central Range on the western side of the nearly vertical LVF is clearly imaged as a high-V_P, high-V_S and low-σ anomaly, whereas the

Coastal Range on the eastern side is imaged as a low-V_P, low-V_S and high-σ anomaly, showing very good agreement with the characteristics obtained by previous studies (Wu et al., 2009; Huang et al., 2014). Although the subducting slabs are not considered in the starting model as *a priori* information, our tomographic results clearly show differences between inside and outside the expected slab bodies; we can see prominent low-V_P, low-V_S and high-σ anomalies above or in between the expected Eurasian and PHS slab bodies. The 2018 and 2019 Hualien mainshock hypocenters are underlain by a low-V_P, low-V_S and high-σ anomaly connecting with the estimated upper boundary of the subducting PHS slab (Fig. 6), which may reflect ascending fluids dehydrated from the slab surface. The Guishan volcano is underlain by a low-V conduit elongating from the slab surface (Fig. 6). Note that the upper boundary of the subducting PHS slab is located at a depth of ~100 km just beneath this volcano (Fig. S6), which is a common characteristic of
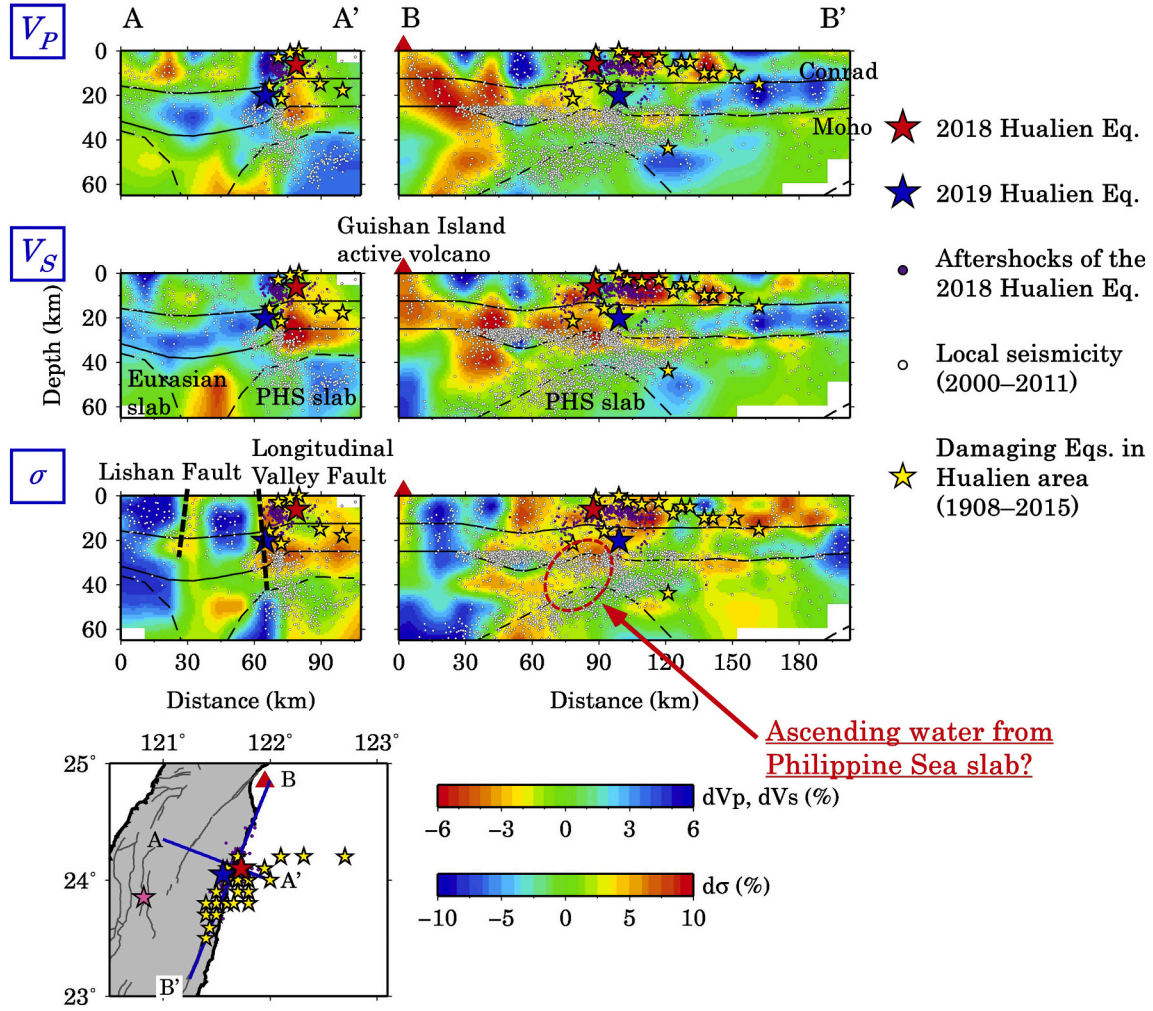
Fig. 6. Vertical cross-sections of *P*-wave velocity (*V_P*, top), *S*-wave velocity (*V_S*, middle), and Poisson's ratio (*σ*, bottom) images along the profiles A-A' (left) and B-B' (right) as shown on the inset map. The vertical exaggeration is 1:1. The red colour denotes low velocity and high Poisson's ratio, whereas the blue colour denotes high velocity and low Poisson's ratio, whose scales (in %) are shown at the bottom. The two black solid lines denote the Conrad and Moho discontinuities, whereas the thin dashed lines show the upper boundaries of the subducting Eurasian and Philippine Sea slabs, expected from Fig. S6. The thick dashed lines denote estimated depth extents of active faults on the surface. The red star denotes the 2018 Hualien hypocenter at 6.3 km depth. The blue star denotes the 2019 Hualien hypocenter at 20.3 km depth. The purple dots denote aftershocks of the 2018 Hualien earthquake. The yellow stars denote the hypocenters of damaging earthquakes (*M* 5.7–8.3) that occurred in the Hualien area during 1908–2015 (Table S1). The white dots denote local seismicity within a 10-km width of each profile. The red triangle denotes the Guishan active volcano. (For interpretation of the references to colour in this figure legend, the reader is referred to the web version of this article.)

the volcanic front in subduction zones (*e.g.*, Tatsumi, 1989; Zhao et al., 1992).

The optimal values of the damping and smoothing parameters (15.0 and 0.02) are found after making many tomographic inversions, a subset of which are shown in Fig. S16. The root-mean-square (RMS) of the total travel-time residuals is 0.345 s for the initial 1-D model, while it is reduced to 0.290 s for the final 3-D model.

4. Resolution tests and control experiments (CEs)

We conducted extensive resolution tests including the checkerboard resolution tests (CRTs) (*e.g.*, Humphreys and Clayton, 1988), restoring resolution test (RRT) (*e.g.*, Zhao et al., 1992; Toyokuni et al., 2016, 2020a) and synthetic resolution tests (SRTs) (*e.g.*, Toyokuni et al., 2016), to assess the spatial resolution and reliability of our tomographic result. The CRTs use an input velocity model that contains alternate positive and negative *V_P* and *V_S* anomalies assigned to the 3-D grid nodes; the amplitude of velocity anomalies is 6% at all the nodes. Two CRTs are performed with a lateral grid interval of 0.1° (CRT1) and 0.2° (CRT2). The RRT highlights the patterns of the tomographic result when

constructing the input model, *i.e.*, at the grid nodes with the *V_P* or *V_S* anomalies > +2.0% or < −2.0% in the tomographic result (Figs. 3 and 4), we put constant *V_P* or *V_S* anomalies of +6% or − 6% for making the RRT input model. The SRTs are similar to the RRT but the input models contain only the high-*V* (SRT1) or low-*V* (SRT2) anomalies. Theoretical arrival times for these input models are calculated with random errors added, which range between −0.2 and + 0.2 s with a standard deviation of 0.1 s. The inversion algorithm and the 3-D grid adopted are the same as those for the real data inversion.

Main features of the test results are summarized in Fig. 8, and the complete test results are shown in the supporting information for CRT1 (Figs. S17 − S20), CRT2 (Figs. S21 − S24), RRT (Figs. S25 and S26), SRT1 (Figs. S27 and S28), and SRT2 (Figs. S29 and S30). For the CRT results, the images of the recovery rate (*e.g.*, Toyokuni et al., 2020b) are also shown. The two CRT results indicate that the resolution in our study region is 0.1° ∼ 0.2° in the horizontal direction, and the vertical resolution is comparable to the grid interval in depth within areas with a hit count ≥50 (Figs. S8 and S9). The RRT and SRTs results also show that the input velocity anomalies in the 2018 and 2019 Hualien source zone are recovered very well. Among the SRTs, the high-*V* anomaly (SRT1)
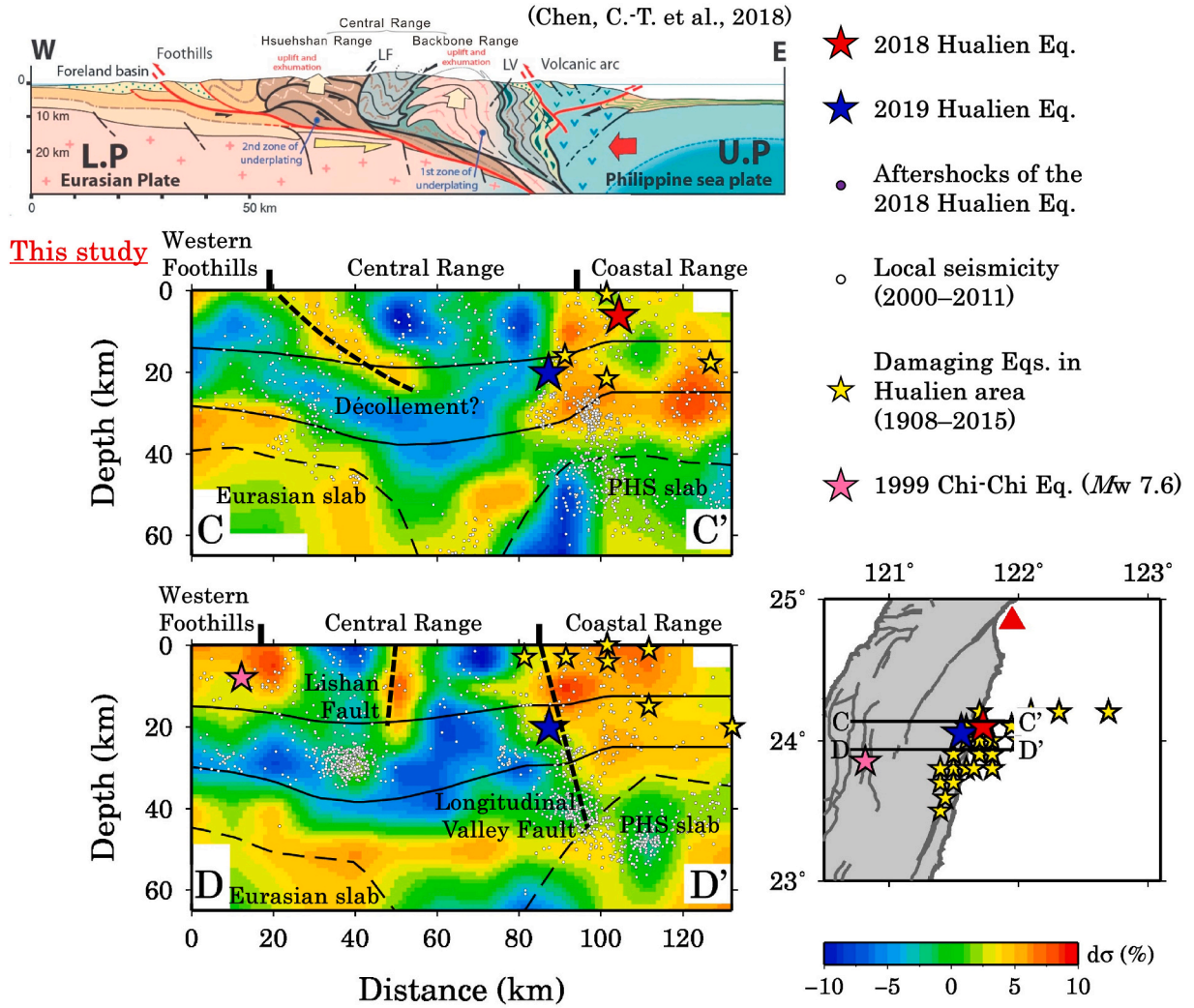
Fig. 7. Comparison of two east-west vertical cross-sections of Poisson's ratio image with an orogenic wedge model (the upper panel; Chen et al., 2018). Locations of the cross-sections (C-C' and D-D') are shown on the inset map. The vertical exaggeration of the tomographic images is 1:1. The red star denotes the 2018 Hualien hypocenter at 6.3 km depth. The blue star denotes the 2019 Hualien hypocenter at 20.3 km depth. The pink star denotes the hypocenter of the 1999 Chi-Chi earthquake. The yellow stars denote the hypocenters of damaging earthquakes (*M* 5.7–8.3) that occurred in the Hualien area during 1908–2015 (Table S1). The white dots denote local seismicity within a 10-km width of each profile. Other labels are the same as those in Fig. 6. (For interpretation of the references to colour in this figure legend, the reader is referred to the web version of this article.)

seems less recovered than the low-*V* anomaly (SRT2). This may be because the high-*V* anomaly is much apparent beneath the oceanic regions where the resolution of the tomographic inversion is relatively poor. Although many previous tomographic studies covered the present study region (*e.g.*, Wu et al., 2009; Huang et al., 2014; Wang and Kao, 2019; Fan and Zhao, 2021), we are able to obtain higher-resolution images due to the finer 3-D grid adopted for inversion and the better data set with carefully selected events.

We also conducted five control experiments (CE1−5) to assess the reliability and robustness of our tomographic results. Main features of the CEs are summarized in Fig. 9, and their complete results are shown in the supporting information for CE1 (Figs. S31 − S35), CE2 (Figs. S36 − S45), CE3 (Figs. S46 − S56), CE4 (Figs. S57 − S67), and CE5 (Figs. S68 − S73).

The CE1 adopts different 3-D grid nodes, which are shifted by 0.05° in both the latitudinal and longitudinal directions from the original grid (Fig. S3). The grid locations in the vertical direction are also different from the original grid; we set up them at depths of 1, 4, 9, 15, 20, 27, 35, 45, 60, and 80 km (Fig. S31). The inversion results show that the overall pattern and main features of the velocity and Poisson's ratio images in and around the Hualien source zone remain the same (Fig. 9b, see also

Figs. S32 − S35).

The CE2 conducts an inversion with a flat Conrad at 12.5 km depth and a flat Moho at 25 km depth, which are the average Conrad and Moho depths in North Taiwan. The inversion results show that the overall pattern of the tomographic images also remains the same (Fig. 9c, see also Figs. S36 − S45), but the final RMS travel-time residual is 0.303 s for the inversion with the flat Conrad and Moho, which is about 4.5% larger than the RMS residual (0.290 s) for the inversion with the curved Conrad and Moho (Figs. 3−7). These results suggest that when the geometries of velocity discontinuities are taken into account, a better 3-D velocity model can be obtained, because the ray paths and theoretical travel times can be computed more accurately (Zhao et al., 1992).

The CE3 takes the 1-D velocity model of Wu et al. (2009) as the initial model. This 1-D model contains very low-*V* layers at the shallow depths and it has no velocity discontinuities (Fig. S46), so the structure of the shallow part (depth ≤ 10 km) changes drastically, showing dominant high-*V* anomalies. However, the main features of the Poisson's ratio images in and around the 2018 and 2019 Hualien hypocenters remain the same (Fig. 9d, see also Figs. S47 − S56).

The CE4 is conducted without the thinning out of the offshore events, *i.e.*, we use all the 24,029 events obtained after the process (3) described
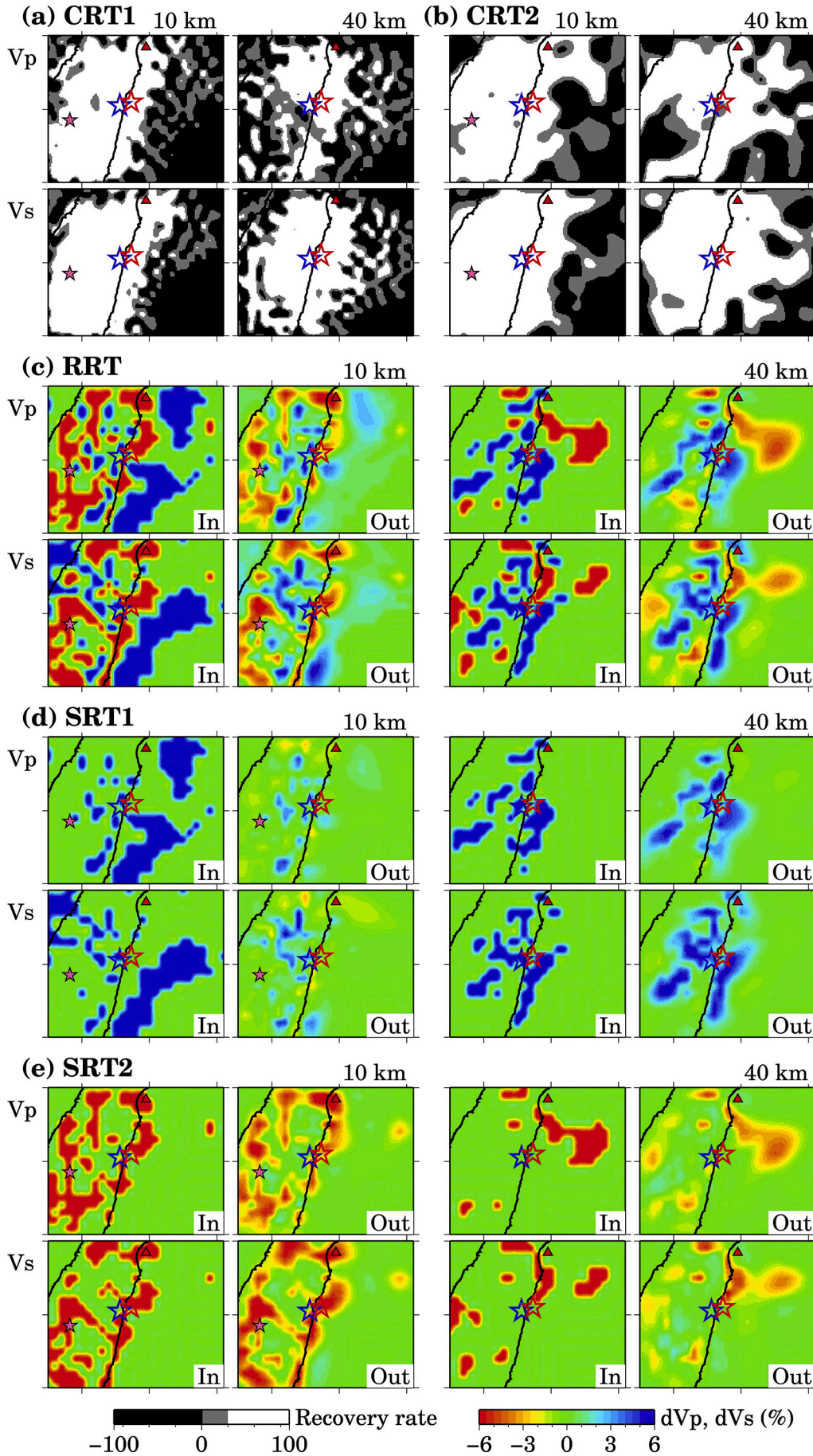
Fig. 8. Summary of the resolution tests. Map view images at depths of 10 km (left panels) and 40 km (right panels) for both V_P (upper panels) and V_S (lower panels). (a) CRT1 recovery rate, (b) CRT2 recovery rate, (c) RRT input (left) and output (right) models, (d) SRT1 input (left) and output (right) models, and (e) SRT2 input (left) and output (right) models, whose scales are shown at the bottom. The red and blue stars denote the epicenters of the 2018 and 2019 Hualien earthquakes, respectively. The pink star denotes the epicenter of the 1999 Chi-Chi earthquake. The red triangle denotes the Guishan active volcano. (For interpretation of the references to colour in this figure legend, the reader is referred to the web version of this article.)
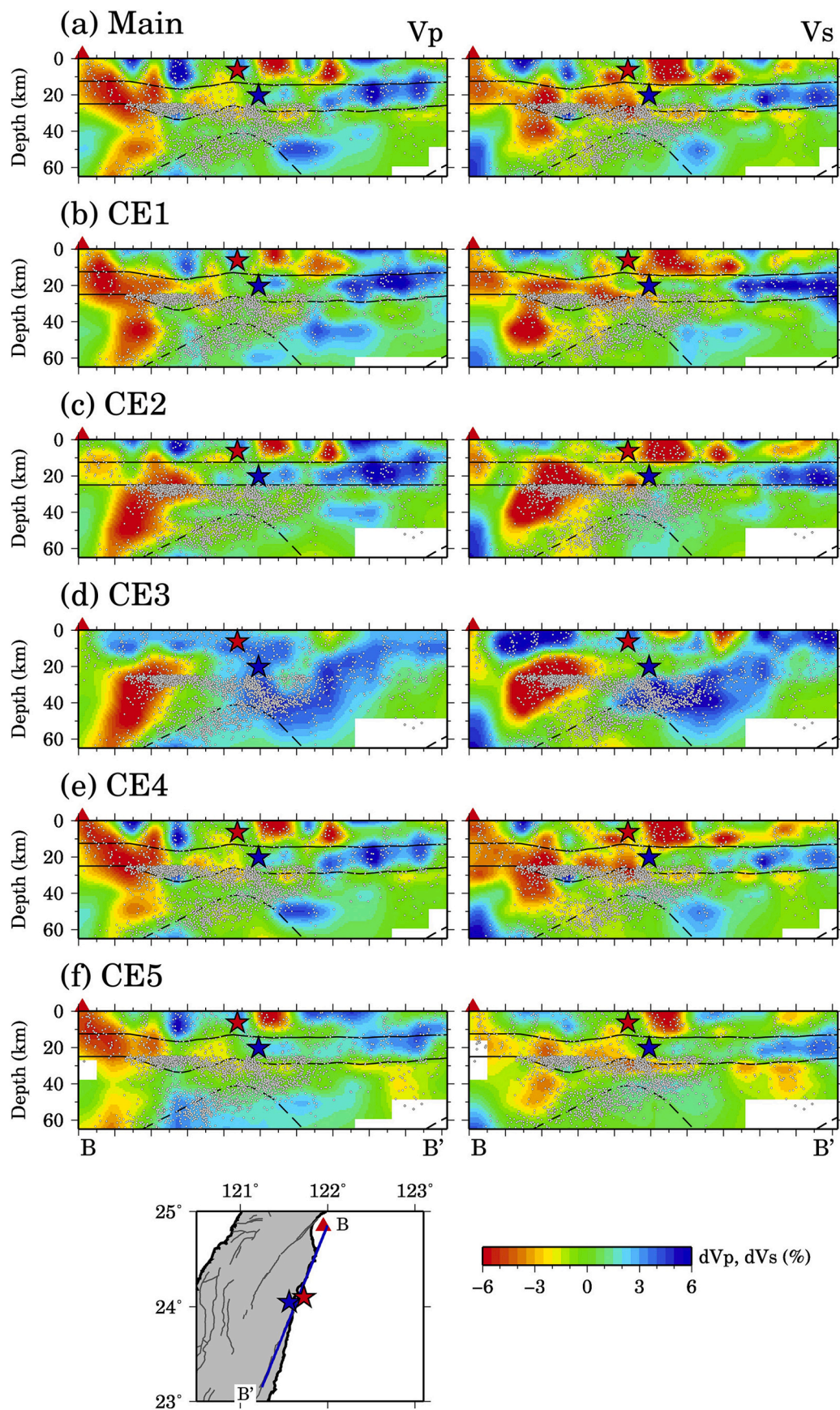
Fig. 9. Summary of the control experiments (CEs). Vertical cross-sections of *P*-wave velocity (V_P, left) and *S*-wave velocity (V_S, right) for (a) main tomographic results, (b) CE1, (c) CE2, (d) CE3, (e) CE4, and (f) CE5, along the profile B-B' as shown on the inset map (the same profile as in Fig. 6). Other labels are the same as those in Fig. 6. (For interpretation of the references to colour in this figure legend, the reader is referred to the web version of this article.)

in Section 2 (Fig. S57). The inversion results show that the overall pattern of the tomographic images is almost the same (Fig. 9e, see also Figs. S58 − S67), which indicates that those offshore events are still usable. However, the final RMS travel-time residual is 0.292 s, which is slightly larger than that for our preferred velocity model (0.290 s), suggesting the higher reliability of the results when those offshore events are removed.

The CE5 conducts an inversion for a smaller target region in the latitude range 23.0°–25.0°N and longitude range 120.5°–122.0°E, which is selected by cutting off the sea area (Fig. S68). In the smaller target region, the ray path coverage around the Hualien source area deteriorates, but we can completely exclude the offshore earthquakes that may have poor hypocentral locations. We used P- and S-wave arrival-time data of 9320 local earthquakes in the smaller target region that were recorded at 46 seismic stations (Fig. S68). We adopted the criteria (1)–(3) in Section 2 for the earthquake extraction. We further discarded offshore earthquakes by a stronger criterion than the criterion (4) in Section 2. The grid distribution is shown in Fig. S69. The inversion results do not show a clear low-V anomaly beneath the active volcano, and do not reveal the coastal low-V anomalous belt at ≤10 km depth as shown in Figs. 3 and 4, suggesting the importance of the data from those offshore events (Fig. 9f, see also Figs. S70 − S73).

5. Discussion and conclusions

The 2018 and 2019 Hualien earthquakes took place at the western edge of a low-V_P, low-V_S and high-σ anomaly at depths of 5–30 km (Fig. 6), indicating the nearly vertical LVF and its shallow sediments separating the Central Range and Coastal Range. Previous studies have suggested that LVF extends nearly vertically from the surface to a depth of ~40 km (e.g., Chen et al., 2019), which supports our results. Focusing on the double-couple component, the two earthquakes mainly exhibit reverse-fault mechanisms. Each of their Harvard CMT solutions (Fig. 1b) has a nodal plane with a high dip angle along the LVF, suggesting the rupture along the LVF and its northward extension.

The high-σ anomaly beneath the source zone of the two earthquakes suggests the existence of crustal fluids, which is also supported by low heat flow (Hsieh et al., 2014), negative Bouguer gravity anomaly (Yen and Hsieh, 2010), and low electrical resistivity (Bertrand et al., 2012) in the region. These results may reflect crustal fluids contained in the volcanoclastic rocks attributed to the suture of the collision in the Coastal Range (Lo et al., 2019). The Guishan active volcano is underlain by a low-V anomaly, but high-σ is not so prominent. Therefore, the crustal fluids associated with the two Hualien earthquakes may be in a separate system from those associated with the Guishan volcano.

The Hualien hypocenters are located just above a site where the upper boundary of the subducting PHS slab becomes unobservable suddenly on the west (Fig. S6). Further to the west, the subducting Eurasian slab is approaching, suggesting that the PHS slab is undergoing sharp bending or tearing in this region. Thus, this region might be in an environment that water contained in the subducted PHS slab is easy to dehydrate from the slab body. Lee et al. (2019) suggested that the non-double couple component was dominant in the focal mechanism of the 2018 Hualien earthquake because of multiple rupture planes and its complex rupture process. The non-double couple component was also dominant in the 2019 Hualien earthquake. Hence, the source zone of these two earthquakes might have structural anomalies that tend to cause the non-double-couple components, rather than just the complexity of rupture process. It is well known that fluids in the source zone, if any, can cause the non-double-couple component of focal mechanisms (e.g., Wang et al., 2018).

The source zone of the two Hualien earthquakes is known as a high compressive-strain-rate zone due to the collision, revealed by GPS-derived surface velocities (Hsu et al., 2009). These results suggest that the generation of the two Hualien earthquakes was affected by the ascending fluids from the subducting slab dehydration, invading into an active fault with a high loading rate. Such a water-bearing feature has been also revealed in large earthquake areas in Japan, India, US, China, and South Taiwan (e.g., Zhao et al., 1996, 2002, 2018; Mishra, 2013; Mishra and Zhao, 2003; Hauksson et al., 2004; Lei and Zhao, 2009; Tong et al., 2012; Toyokuni et al., 2016).

Our vertical cross-sections show that the 1999 Chi-Chi earthquake (Mw 7.6) and other damaging earthquakes occurred in the Hualien area from 1908 to 2015, including the 1951 Hualien earthquake (M_L 7.3) (Table S1). The hypocentral locations of the offshore historical earthquakes have some uncertainties, but we can see that most of the damaging earthquakes occurred in the high-V zone or at the boundary between the high-V and low-V zones. Such a feature has been broadly observed in the world, e.g., in the megathrust zone under the NE Japan forearc (Zhao et al., 2011; Hua et al., 2020). The 1999 Chi-Chi hypocenter is also located at the boundary between a shallow low-σ anomaly and a deep high-σ anomaly, indicating the invading crustal fluids (see the E-E' section in Fig. S12 and the G-G' section in Fig. S15). This large earthquake is known as a thrust event (e.g. Wang et al., 2000; Seno et al., 2000) that might be caused by a different mechanism from that of the two Hualien earthquakes, but we deem that crustal fluids play an important role in the generation of most (if not all) large earthquakes in the Taiwan orogeny.

Author contributions

G.T. and D.Z. designed this study. G.T. conducted data processing and inversion. G.T. and D.Z. wrote the manuscript. K.H.C. provided arrival-time data. All authors contributed to the interpretations and preparation of the manuscript.

Declaration of Competing Interest

The authors declare that they have no known competing financial interests or personal relationships that could have appeared to influence the work reported in this paper.

Acknowledgments

Appendix A. Supplementary data

Supplementary data to this article can be found online at https://doi.org/10.1016/j.pepi.2021.106673.

References

Bertrand, E.A., Unsworth, M.J., Chiang, C.-W., Chen, C.-S., Chen, C.-C., Wu, F.T., Türkoğlu, E., Hsu, H.-L., Hill, G.J., 2012. Magnetotelluric imaging beneath the Taiwan orogen: An arc-continent collision. J. Geophys. Res. 117, B01402 https://doi.org/10.1029/2011JB008688.

Chai, B.H.T., 1972. Structure and tectonic evolution of Taiwan. Am. J. Sci. 272, 389–422. https://doi.org/10.2475/ajs.272.5.389.

Chen, C.-T., Chan, Y.-C., Lo, C.-H., Malavieille, J., Lu, C.-Y., Tang, J.-T., Lee, Y.-H., 2018. Basal accretion, a major mechanism for mountain building in Taiwan revealed in rock thermal history. J. Asian Earth Sci. 152, 80–90. https://doi.org/10.1016/j.jseaes.2017.11.030.

Chen, A.-T., Shen, C.-C., Byrne, T.B., Sano, Y., Takahata, N., Yang, T.F., Wang, Y., 2019. Mantle fluids associated with crustal-scale faulting in a continental subduction setting, Taiwan. Sci. Rep. 9, 10805. https://doi.org/10.1038/s41598-019-47070-2.

Fan, J., Zhao, D., 2021. P-wave tomography and azimuthal anisotropy of the Manila-Taiwan-southern Ryukyu region. Tectonics 40. https://doi.org/10.1029/2020TC006262 e2020TC006262.

Hauksson, E., Oppenheimer, D., Brocher, T.M., 2004. Imaging the source region of the 2003 San Simeon earthquake within the weak Franciscan subduction complex, central California. Geophys. Res. Lett. 31, L20607 https://doi.org/10.1029/2004GL021049.

Ho, C.S., 1988. An Introduction to the Geology of Taiwan: Explanatory Text of the Geology Map of Taiwan, 2nd ed. Ministry of Economic Affairs, R.O.C. 192 pp.

Hsieh, H.-H., Chen, C.-H., Lin, P.-Y., Yen, H.-Y., 2014. Curie point depth from spectral analysis of magnetic data in Taiwan. J. Asian Earth Sci. 90, 26–33. https://doi.org/10.1016/j.jseaes.2014.04.007.

Hsu, Y.-J., Yu, S.-B., Simons, M., Kuo, L.-C., Chen, H.-Y., 2009. Interseismic crustal deformation in the Taiwan plate boundary zone revealed by GPS observations, seismicity, and earthquake focal mechanisms. Tectonophysics 479, 4–18. https://doi.org/10.1016/j.tecto.2008.11.016.

Hsu, H.-J., Wen, S., Chen, C.-H., 2011. 3D topography of the Moho discontinuity in the Taiwan area as extracted from travel time inversion of PmP phases. J. Asian Earth Sci. 41, 335–343. https://doi.org/10.1016/j.jseaes.2011.02.003.

Hua, Y., Zhao, D., Toyokuni, G., Xu, Y., 2020. Tomography of the source zone of the great 2011 Tohoku earthquake. Nat. Commun. 11, 1163. https://doi.org/10.1038/s41467-020-14745-8.

Huang, M.-H., Huang, H.-H., 2018. The complexity of the 2018 Mw 6.4 Hualien earthquake in East Taiwan. Geophys. Res. Lett. 45, 13249–13257. https://doi.org/10.1029/2018GL080821.

Huang, H.-H., Wu, Y.-M., Song, X., Chang, C.-H., Lee, S.-J., Chang, T.-M., Hsieh, H.-H., 2014. Joint Vp and Vs tomography of Taiwan: Implications for subduction-collision orogeny. Earth Planet. Sci. Lett. 392, 177–191. https://doi.org/10.1016/j.epsl.2014.02.026.

Huang, S.-Y., Yen, J.-Y., Wu, B.-L., Yen, I.-C., Chuang, R.Y., 2019. Investigating the Milun Fault: The coseismic surface rupture zone of the 2018/02/06 M_L 6.2 Hualien earthquake, Taiwan. Terr. Atmos. Ocean. Sci. 30, 311–335. https://doi.org/10.3319/TAO.2018.12.09.03.

Humphreys, E., Clayton, R.W., 1988. Adaptation of back projection tomography to seismic travel time problems. J. Geophys. Res. 93 (B2), 1073–1085. https://doi.org/10.1029/JB093iB02p01073.

Lee, S.-J., Lin, T.-C., Liu, T.-Y., Wong, T.-P., 2019. Fault-to-fault jumping rupture of the 2018 Mw 6.4 Hualien earthquake in eastern Taiwan. Seismol. Res. Lett. 90, 30–39. https://doi.org/10.1785/0220180182.

Lei, J., Zhao, D., 2009. Structural heterogeneity of the Longmenshan fault zone and the mechanism of the 2008 Wenchuan earthquake (Ms 8.0). Geochem. Geophys. Geosyst. 10, Q10010. https://doi.org/10.1029/2009GC002590.

Lin, A.T., Watts, A.B., 2002. Origin of the West Taiwan basin by orogenic loading and flexure of a rifted continental margin. J. Geophys. Res. 107, 2185. https://doi.org/10.1029/2001JB000669.

Lin, Y.-S., Chuang, R.Y., Yen, J.-Y., Chen, Y.-C., Kuo, Y.-T., Wu, B.-L., Huang, S.-Y., Yang, C.-J., 2019. Mapping surface breakages of the 2018 Hualien earthquake by using UAS photogrammetry. Terr. Atmos. Ocean. Sci. 30, 351–366. https://doi.org/10.3319/TAO.2018.12.09.02.

Lo, Y.-C., Yue, H., Sun, J., Zhao, L., Li, M., 2019. The 2018 Mw 6.4 Hualien earthquake: Dynamic slip partitioning reveals the spatial transition from mountain building to subduction. Earth Planet. Sci. Lett. 524, 115729. https://doi.org/10.1016/j.epsl.2019.115729.

Mishra, O.P., 2013. Crustal heterogeneity in bulk velocity beneath the 2001 Bhuj earthquake source zone and its implications. Bull. Seismol. Soc. Am. 103, 3235–3247. https://doi.org/10.1785/0120110144.

Mishra, O.P., Zhao, D., 2003. Crack density, saturation rate and porosity at the 2001 Bhuj, India, earthquake hypocenter: a fluid-driven earthquake? Earth Planet. Sci. Lett. 212, 393–405. https://doi.org/10.1016/S0012-821X(03)00285-1.

Seno, T., Stein, S., Gripp, A.E., 1993. A model for the motion of the Philippine Sea Plate consistent with NUVEL-1 and geological data. J. Geophys. Res. 98, 17941–17948. https://doi.org/10.1029/93JB00782.

Seno, T., Otsuki, K., Yang, C.-N., 2000. The 1999 Chi-Chi, Taiwan earthquake: A subduction zone earthquake on land. Bull. Earthq. Res. Inst. Univ. Tokyo 75, 57–77.

Tatsumi, Y., 1989. Migration of fluid phases and genesis of basalt magmas in subduction zones. J. Geophys. Res. 94, 4697–4707. https://doi.org/10.1029/JB094iB04p04697.

Teng, L.S., 1990. Geotectonic evolution of late Cenozoic arc-continent collision in Taiwan. Tectonophysics 183, 57–76. https://doi.org/10.1016/0040-1951(90)90188-E.

Tong, P., Zhao, D., Yang, D., 2012. Tomography of the 2011 Iwaki earthquake (M 7.0) and Fukushima nuclear power plant area. Solid Earth 3, 43–51. https://doi.org/10.5194/se-3-43-2012.

Toyokuni, G., Zhao, D., Chen, K.H., 2016. Tomography of the source zone of the 2016 South Taiwan earthquake. Geophys. J. Int. 207, 635–643. https://doi.org/10.1093/gji/ggw304.

Toyokuni, G., Matsuno, T., Zhao, D., 2020a. *P wave* tomography beneath Greenland and surrounding regions: 1. Crust and upper mantle. J. Geophys. Res. Solid Earth 125. https://doi.org/10.1029/2020JB019837 e2020JB019837.

Toyokuni, G., Matsuno, T., Zhao, D., 2020b. *P wave* tomography beneath Greenland and surrounding regions: 2. Lower mantle. J. Geophys. Res. Solid Earth 125. https://doi.org/10.1029/2020JB019839 e2020JB019839.

Tung, H., Chen, H.-Y., Hsu, Y.-J., Hu, J.-C., Chang, Y.-H., Kuo, Y.-T., 2019. Triggered slip on multifaults after the 2018 Mw 6.4 Hualien earthquake by continuous GPS and InSAR measurements. Terr. Atmos. Ocean. Sci. 30, 285–300. https://doi.org/10.3319/TAO.2019.04.03.01.

Ustaszewski, K., Wu, Y.-M., Suppe, J., Huang, H.-H., Chang, C.-H., Carena, S., 2012. Crust–mantle boundaries in the Taiwan–Luzon arc-continent collision system determined from local earthquake tomography and 1D models: Implications for the mode of subduction polarity reversal. Tectonophysics 578, 31–49. https://doi.org/10.1016/j.tecto.2011.12.029.

Wang, Z., Kao, H., 2019. The significance of tomographic edge zones for large earthquakes in Taiwan. J. Geophys. Res. Solid Earth 124, 11822–11839. https://doi.org/10.1029/2019JB017875.

Wang, C.-Y., Chang, C.-H., Yen, H.-Y., 2000. An interpretation of the 1999 Chi-Chi earthquake in Taiwan based on the thin-skinned thrust model. Terr. Atmos. Ocean. Sci. 11, 609–630. https://doi.org/10.3319/TAO.2000.11.3.609(CCE).

Wang, Z., Zhao, D., Wang, J., Kao, H., 2006. Tomographic evidence for the Eurasian lithosphere subducting beneath south Taiwan. Geophys. Res. Lett. 33, L18306 https://doi.org/10.1029/2006GL027166.

Wang, R., Gu, Y.J., Schultz, R., Chen, Y., 2018. Faults and non-double-couple components for induced earthquakes. Geophys. Res. Lett. 45, 8966–8975. https://doi.org/10.1029/2018GL079027.

Wessel, P., Smith, W.H.F., Scharroo, R., Luis, J., Wobbe, F., 2013. Generic Mapping Tools: Improved version released. Eos Trans. AGU 94, 409. https://doi.org/10.1002/2013EO450001.

Wu, Y.-M., Shyu, J.B.H., Chang, C.-H., Zhao, L., Nakamura, M., Hsu, S.-K., 2009. Improved seismic tomography offshore northeastern Taiwan: Implications for subduction and collision processes between Taiwan and the southernmost Ryukyu. Geophys. J. Int. 178, 1042–1054. https://doi.org/10.1111/j.1365-246X.2009.04180.x.

Wu, B.-L., Yen, J.-Y., Huang, S.-Y., Kuo, Y.-T., Chang, W.-Y., 2019. Surface deformation of 0206 Hualien earthquake revealed by the integrated network of RTK GPS. Terr. Atmos. Ocean. Sci. 30, 301–310. https://doi.org/10.3319/TAO.2019.05.27.01.

Yamada, M., Cho, I., Kuo, C.-H., Lin, C.-M., Miyakoshi, K., Guo, Y., Hayashida, T., Matsumoto, Y., Mori, J., Yen, Y.-T., Kuo, K.-C., 2020. Shallow subsurface structure in the Hualien basin and relevance to the damage pattern and fault rupture during the 2018 Hualien earthquake. Bull. Seismol. Soc. Am. 110, 2939–2952. https://doi.org/10.1785/0120200063.

Yen, H.-Y., Hsieh, H.-H., 2010. A study on the compatibility of 3-D seismic velocity structures with gravity data of Taiwan. Terr. Atmos. Ocean. Sci. 21, 897–904. https://doi.org/10.3319/TAO.2010.03.03.01(T).

Yu, S.-B., Chen, H.-Y., Kuo, L.-C., 1997. Velocity field of GPS stations in the Taiwan area. Tectonophysics 274, 41–59. https://doi.org/10.1016/S0040-1951(96)00297-1.

Zhao, D., Hasegawa, A., Horiuchi, S., 1992. Tomographic imaging of P and S wave velocity structure beneath northeastern Japan. J. Geophys. Res. 97, 19909–19928. https://doi.org/10.1029/92JB00603.

Zhao, D., Kanamori, H., Negishi, H., Wiens, D., 1996. Tomography of the source area of the 1995 Kobe earthquake: Evidence for fluids at the hypocenter? Science 274, 1891–1894. https://doi.org/10.1126/science.274.5294.1891.

Zhao, D., Mishra, O.P., Sanda, R., 2002. Influence of fluids and magma on earthquakes: seismological evidence. Phys. Earth Planet. Inter. 132, 249–267. https://doi.org/10.1016/S0031-9201(02)00082-1.

Zhao, D., Huang, Z., Umino, N., Hasegawa, A., Kanamori, H., 2011. Structural heterogeneity in the megathrust zone and mechanism of the 2011 Tohoku-oki earthquake (Mw 9.0). Geophys. Res. Lett. 38, L17308. https://doi.org/10.1029/2011GL048408.

Zhao, D., Liu, X., Hua, Y., 2018. Tottori earthquakes and Daisen volcano: Effects of fluids, slab melting and hot mantle upwelling. Earth Planet. Sci. Lett. 485, 121–129. https://doi.org/10.1016/j.epsl.2017.12.040.